

THE LUMINOSITIES OF THE COLDEST BROWN DWARFS*

C. G. TINNEY^{A,B}, JACQUELINE K. FAHERTY^C, J. DAVY KIRKPATRICK^D, MIKE CUSHING^E, CAROLINE V. MORLEY^F, EDWARD L. WRIGHT^G

(Received 8 July, 2014; Accepted 2 October, 2014)
To appear in The Astrophysical Journal

ABSTRACT

In recent years brown dwarfs have been extended to a new Y-dwarf class with effective temperatures colder than 500K and masses in the range 5-30 Jupiter masses. They fill a crucial gap in observable atmospheric properties between the much colder gas-giant planets of our own Solar System (at around 130K) and both hotter T-type brown dwarfs and the hotter planets that can be imaged orbiting young nearby stars (both with effective temperatures of in the range 1500-1000K). Distance measurements for these objects deliver absolute magnitudes that make critical tests of our understanding of very cool atmospheres. Here we report new distances for nine Y dwarfs and seven very-late T dwarfs. These reveal that Y dwarfs do indeed represent a continuation of the T dwarf sequence to both fainter luminosities and cooler temperatures. They also show that the coolest objects display a large range in absolute magnitude for a given photometric colour. The latest atmospheric models show good agreement with the majority of these Y dwarf absolute magnitudes. This is also the case for WISE0855-0714 the coldest and closest brown dwarf to the Sun, which shows evidence for water ice clouds. However, there are also some outstanding exceptions, which suggest either binarity or the presence of condensate clouds. The former is readily testable with current adaptive optics facilities. The latter would mean that the range of cloudiness in Y dwarfs is substantial with most hosting almost no clouds – while others have dense clouds making them prime targets for future variability observations to study cloud dynamics.

Subject headings: Brown dwarfs; Techniques: photometric; Methods: observational

1. INTRODUCTION

Y-type brown dwarfs were first discovered by the WISE satellite (Cushing et al. 2011) as an extension to colder temperatures of the L- and T-type sequences for stars and brown dwarfs⁹ (Reid & Hawley 2006). Interpretation of the physical properties of these unusual objects has been primarily driven by modelling of their observed spectra (Kirkpatrick et al. 2013; Cushing et al. 2011; Leggett et al. 2013) using a variety of atmospheric models (Allard et al. 2003; Saumon & Marley 2008; Morley et al. 2014). However, while the interior structures for brown dwarfs are relatively straightforward (Stevenson 1991), atmospheres represent a substantial challenge. At these very cold temperatures a rich panoply of molecular

physics in a wide range of species (including CO, CH₄, N₂, NH₃, H₂O, Fe, Cr, CaTiO₃, Na₂S, MnS, ZnS and KCl) becomes critical – not only for modelling the opacity as a function of wavelength through the atmosphere, but also for determining the physical structure of the atmosphere (i.e. whether condensates are present), as well as the atmosphere’s chemical make-up. Since condensed molecules are removed from the gas-phase chemistry, their absorption opacities are removed from the radiative transfer, but have to be accounted for in the form of clouds of scatterers and absorbers. The physical height at which cloud layers of various materials will settle (as a function of each object’s overall effective temperature and specific atmospheric structure) therefore becomes a vital component of atmospheric models.

Examples of the impact of such cloud formation on the emergent spectra of brown dwarfs include: the evolution of observable molecular bands of TiO, VO and FeH through the L dwarf sequence (Tsuji 2000); the transition from cloudy late L-dwarfs to relatively cloudless early T dwarfs (the specific mechanism for which is still hotly debated, and which allows significant rotationally-driven variability at this transition Saumon & Marley 2008; Radigan et al. 2012; Artigau et al. 2009); and the associated increase in the J-band absolute magnitude (the “J-band hump”) seen in early T dwarfs (Tinney et al. 2003).

Distance measurements via trigonometric parallaxes have been key in determining the physics required in succeeding generations of models, since they provide absolute magnitudes (in a given bandpass), which can be integrated to determine bolometric luminosities. They are also key for completing the census of objects near

* This paper includes data gathered with the 6.5 meter Magellan Telescopes located at Las Campanas Observatory, Chile.

^a School of Physics, UNSW Australia, NSW 2052, Australia. c.tinney@unsw.edu.au

^b Australian Centre for Astrobiology, UNSW Australia, NSW 2052, Australia

^c Department of Terrestrial Magnetism, Carnegie Institution of Washington, Washington DC, USA

^d Infrared Processing and Analysis Center, MS100-22, California Institute of Technology, Pasadena, CA 91125, USA

^e Department of Physics and Astronomy, The University of Toledo, OH 43606, USA

^f Department of Astronomy and Astrophysics, University of California, Santa Cruz, CA 95064, USA

^g Department of Physics and Astronomy, UCLA, Los Angeles, CA 90095-1547, USA

⁹ We note also the detection of the companion to the white dwarf WD 0806-661 by Luhman et al. (2011), and the detection of a faint companion in the CFBDIRS J1458+1013AB system (Liu et al. 2011b). Though both these objects (like W0855 discovered by Luhman 2014) are too faint to allow an optical or near-infrared spectrum to be obtained, they are very likely Y dwarfs.

the Sun – as spectacularly demonstrated by the recent detection of a 250K brown dwarf at a distance of just 2.2 pc (Luhman 2014).

The astrometric motions produced by trigonometric parallax are small – 40 milliarcseconds (mas) in amplitude for an object at 25 pc. However, techniques have advanced tremendously over the last two decades, and these observations are now possible with ground-based telescopes in both the optical (Monet *et al.* 1992; Dahn *et al.* 2002; Tinney *et al.* 1995) and near-infrared (Tinney *et al.* 2003; Vrba *et al.* 2004; Faherty *et al.* 2012; Dupuy & Liu 2012), as well as using space-based facilities like *Spitzer* and HST (Dupuy & Kraus 2013; Beichman *et al.* 2014).

The *Gaia*¹⁰ mission is set to deliver an unprecedented flood of new astrometry at optical wavelengths over the next few years. However for the coldest brown dwarfs, the combination of their faintness and their flux primarily emerging in the near-to-mid-infrared, means that their parallaxes will remain the exclusive domain of targeted astrometric programs (Smart 2014). In 2012 we therefore commenced a new astrometric program using the FourStar imaging camera on the 6.5m Magellan Baade telescope to target parallax measurements for very faint ($J \sim 19.5\text{--}22$) Y dwarfs.

2. OBSERVATIONS & ANALYSIS

Parallax observations were obtained using the FourStar imaging camera (Persson *et al.* 2008) on the Magellan Baade telescope between March 10, 2012 and June 18, 2014. FourStar is a near-infrared mosaic imager with four 2048×2048 pixel detectors giving an imaging field of view of 11′ on a side at a pixel scale of 0.159″/pixel. It is equipped with a set of intermediate-band filters (originally specified for the measurement of photometric redshifts) which turn out to be almost ideally suited for observing very cool brown dwarfs (see Fig.1 in Tinney *et al.* 2012). In particular, the J3 filter ($\lambda_{cen} \approx 1.29 \mu\text{m}$) collects almost all of the J-band flux from late-T and Y dwarfs, while only collecting roughly half the night-sky emission of the J-band. All imaging results in this paper were obtained in the FourStar J3 filter.

Image quality over the course of the program varied between 0.29″ and 1.19″ with a median of 0.61″ (see Table 1). Our astrometric observing and analysis techniques follow those previously described by us (Tinney *et al.* 2012, 1995), and involve observing each target with the FourStar J3 filter in a sequence of 60–120s randomly dithered exposures at very similar hour angles on every night. Targets are observed reaching net integration times ranging from 15 minutes (for the brightest $J \sim 19$ targets) to 1.5–2.0h (for the faintest $J \sim 22$ targets). Images are dark subtracted, flat-fielded and mosaic-combined in a standard manner using a modified version of the ORACDR¹¹ data reduction pipeline. This is run twice on each field. Individual images revealed to have significantly poorer image quality than the rest of the jittered data set after the first-pass processing are removed from the list of images used in the second-pass.

2.1. Photometric Analysis

¹⁰ <http://sci.esa.int/gaia/>

¹¹ <http://www.jach.hawaii.edu/JACpublic/UKIRT/software/oracdr>

TABLE 1
OBSERVATION EPOCHS AT THE MAGELLAN BAADE
TELESCOPE.

UT Date	Median Seeing (″)	UT Date	Median Seeing (″)
2012 Mar 10	0.64	2013 Jul 27	0.81
2012 May 10	0.56	2013 Aug 15	0.43
2012 Jun 6	0.70	2013 Oct 20	0.84
2012 Jun 7	0.53	2013 Nov 14	0.69
2012 Aug 10	0.87	2013 Dec 11	0.51
2012 Oct 6	0.82	2014 Jan 13	0.74
2013 Jan 15	0.34	2014 Mar 10	0.50
2013 Feb 2	0.92	2014 May 13	0.58
2013 Mar 22	0.32	2014 Jun 17	0.53
2013 Apr 22	0.54	2014 Jun 18	0.54

Photometry for all our targets was measured using Sextractor aperture photometry (Bertin & Arnouts 1996). Each image has been zero-point calibrated by using 2MASS Point Source Catalogue (Skrutskie *et al.* 2006) J-band data in that field to generate a photometric zero point on the J3 photometric system (see below for details). The multiple epoch observations generate multiple J3 photometric estimates for each target, which have been averaged (weighted by estimated photometric uncertainties) to generate J3 photometry for our targets which we report in Table 2 (where the uncertainties quoted are the resulting standard error in the mean). The table also presents literature J_{MKO} photometry for each target where available, along with the full *AllWISE* designations and W2 photometry of each target (Wright *et al.* 2010; Mainzer *et al.* 2011).

Because the J3 filter collects essentially *all* of the flux emitted in the J band for these late T and Y dwarfs, J3 magnitudes can be readily converted to J_{MKO} magnitudes. We have used our new J3 data to update the estimate for this correction presented by Tinney *et al.* (2012). In Figure 1 we plot $J_{MKO}\text{--}J3$ as a function of $J3\text{--}W2$ for the nine objects in Table 2 with J_{MKO} measured to better than 0.2 mag precision. T and Y dwarfs are plotted with different symbols, and the mean value of $J_{MKO}\text{--}J3 = 0.20 \pm 0.03$ (where the uncertainty is the standard error in the mean) is plotted as a dot-dashed line. The data display no evidence for a significant systematic trend (i.e. greater than 0.1 mag in size) over the colour range of interest for Y dwarfs and the latest T dwarfs.

Our J3 data generally has much better photometric precision than the extant J_{MKO} photometry for these objects, and is derived from multiple observations, so we use this corrected J3 photometry to generate “synthetic” J_{MKO} photometry for all our Magellan targets, and we use this photometry whenever we refer to J_{MKO} for those objects in the rest of this paper.

2.2. Astrometric Analysis

Astrometry of our targets was performed following the procedures adopted in earlier astrometric papers by our team (Tinney *et al.* 2012, 2003, 1995). Briefly, astrometry was measured using the DAOPHOT II package (Stetson 1987) as implemented within the Starlink environment provided by the Joint Astronomy Centre,

Hawaii¹². Each epoch is transferred to a master frame using a “solid body” linear transformation that allows for field rotation, plate scale change and field offset (but *not* field shear). The master frame is rotated to the cardinal directions and its plate scale is determined using 2MASS reference stars in the field. Typical uncertainties on the plate scale for the master frame are better than $\pm 0.2\%$ making this a negligible source of uncertainty for the very nearby stars targeted in this program. Astrometric solutions are derived using codes previously developed by us, and making use of the NOVAS library¹³ provided by the US Naval Observatory.

One substantial difference between these observations and those used in our previous parallax programs is that our targets are often substantially fainter than our reference frame stars. As such, using the residuals about each transformation as an estimate for the astrometric uncertainty in each frame (as done by us in the past) does not correctly reflect the full systematic plus photon-counting uncertainties associated with each frame. We therefore carried out an additional analysis using the residuals for all objects present in all frames for a given target (including star-like objects much fainter than the astrometric reference stars). Using the residuals for all these “pseudo-reference” stars, binned as a function of magnitude, we were able to fit a model for the astrometric uncertainty as a function of J3 magnitude in each frame. This model assumes the sky noise over the object photon-counting noise for each target and is of the form

$$\text{RMS}^2 = a_0^2(1 + 10^{0.8(J3-a_1)})$$

Where J3 is the object magnitude, and a_0 and a_1 are fitting constants, such that a_0 parametrises the underlying systematic residuals associated with each frame’s transformation, while a_1 parametrises the precision as a function of magnitude (it is formally the magnitude at which the photon-counting contribution to the precision is equal to the underlying precision of the reference frame transformation a_0). This model was then used to estimate the astrometric precision for our target object in each frame, and these uncertainties are used in the parallax solution.

3. RESULTS

Astrometric parameters are presented in Table 2 along with the number of epochs (N_{epoch}) included in each solution. Plots of the astrometric solutions are shown in Fig. 2 (with proper motions removed for clarity). These show the baseline of the observations obtained, the observation epochs for each target, and the scatter ($\sigma_\alpha, \sigma_\delta$) and reduced chi-squared (χ_ν^2) about each solution.

As W1141 has no extant spectral type, we have used its absolute magnitudes ($M_{W2}=14.68$ and $M_J=19.81$) to estimate that it would have an equivalent spectral type of Y0 ± 1 sub-type (the eleven other Y0 dwarfs with extant absolute magnitude estimates have median values of $M_{W2}=14.65$ and $M_J=20.32$).

The parallax estimates for W0535, W0647 and W2325 are considered preliminary, being based on less than 6 epochs and delivering parallax precisions of greater than 10 mas. Observations for these targets are continuing.

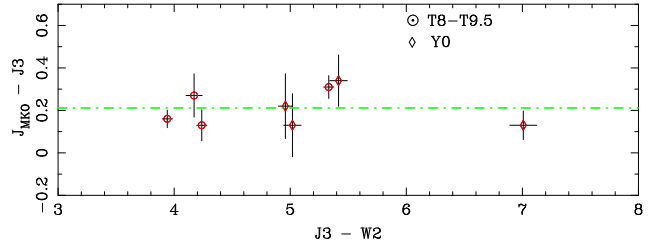


FIG. 1.— $J_{MKO}-J3$ as a function of J3–W2 colour. T dwarfs and Y dwarfs are plotted with distinct symbols, and the mean value of $J_{MKO}-J3$ is indicated by the dot-dashed line.

The quality of the solutions is visibly quite good. There is a noticeable trend for the brightest sources (e.g. W0148, W0713, W1042, W1141, W2102, W2332 with $J3 \lesssim 19.5$) to have χ_ν^2 systematically below 1, suggesting that the procedure for estimating per-epoch uncertainties for the brightest targets may be over estimating these uncertainties. The impact of this over-estimation is that our final parallax and proper-motion uncertainties are likely to be conservative.

There are two solutions which require further discussion. W1639’s uncertainties are systematically *underestimated* as this Y dwarf’s astrometry requires a simultaneous point-spread function fit with a nearby much brighter star (for images of the field see Tinney et al. 2012). The increased uncertainties associated with this joint solution at each epoch will not be reflected in the scatter about the (isolated) reference stars. Since this scatter is used to derive the per-epoch uncertainty for W1639, this will result in underestimated per-epoch uncertainties and an artificially high χ_ν^2 . Similarly, W1541, is currently undergoing a passage past a star 2.5 magnitudes brighter and $1''$ to the south. In this case the “contamination” of the astrometry is so pronounced in the declination direction that the parallax solution is determined by the right ascension component alone – for all other objects it is determined from both the declination and right ascension solutions.

3.1. Other Data

Table 2 provides photometric and parallax data for Y dwarfs with previously published parallaxes due to Dupuy & Kraus (hereafter D&K13 2013), Kirkpatrick et al. (2013, hereafter K13), Beichman et al. (2014, hereafter B14) and most recently for W0855 by Luhman (2014, hereafter L14), as well as for a reference sample of previously published late-T dwarfs. The reference sample of late T dwarfs has been extracted from the literature focussing on those objects with extant spectra (and so spectral types), parallaxes with better than 10% precision and J_{MKO} photometry. It does not aim to be a complete sample of all T dwarfs, but rather a comparison sample of known T dwarfs with high quality data. Sources for the astrometry, spectral types and photometry for these objects are provided in the Table. Photometry for these objects tends to fall into two classes: lower precision data acquired to identify and classify sources via J–W2 colours (e.g. Kirkpatrick et al. 2012; Cushing et al. 2011) and deeper data acquired to obtain bet-

¹² <http://starlink.jach.hawaii.edu/starlink>

¹³ http://aa.usno.navy.mil/software/novas/novas_info.php

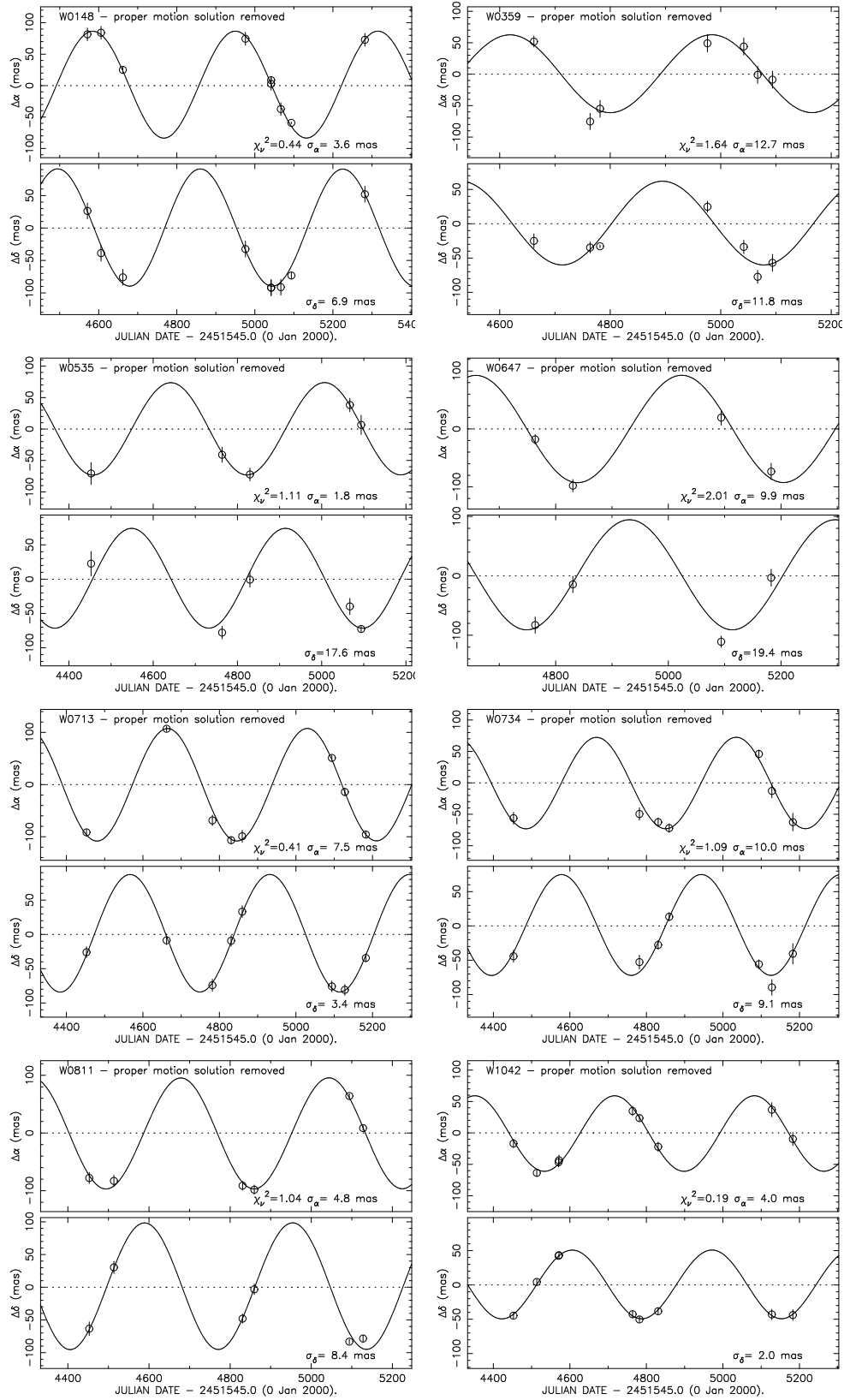


FIG. 2.— Astrometric solutions as reported in Table 2, with the fitted proper motion removed for clarity.

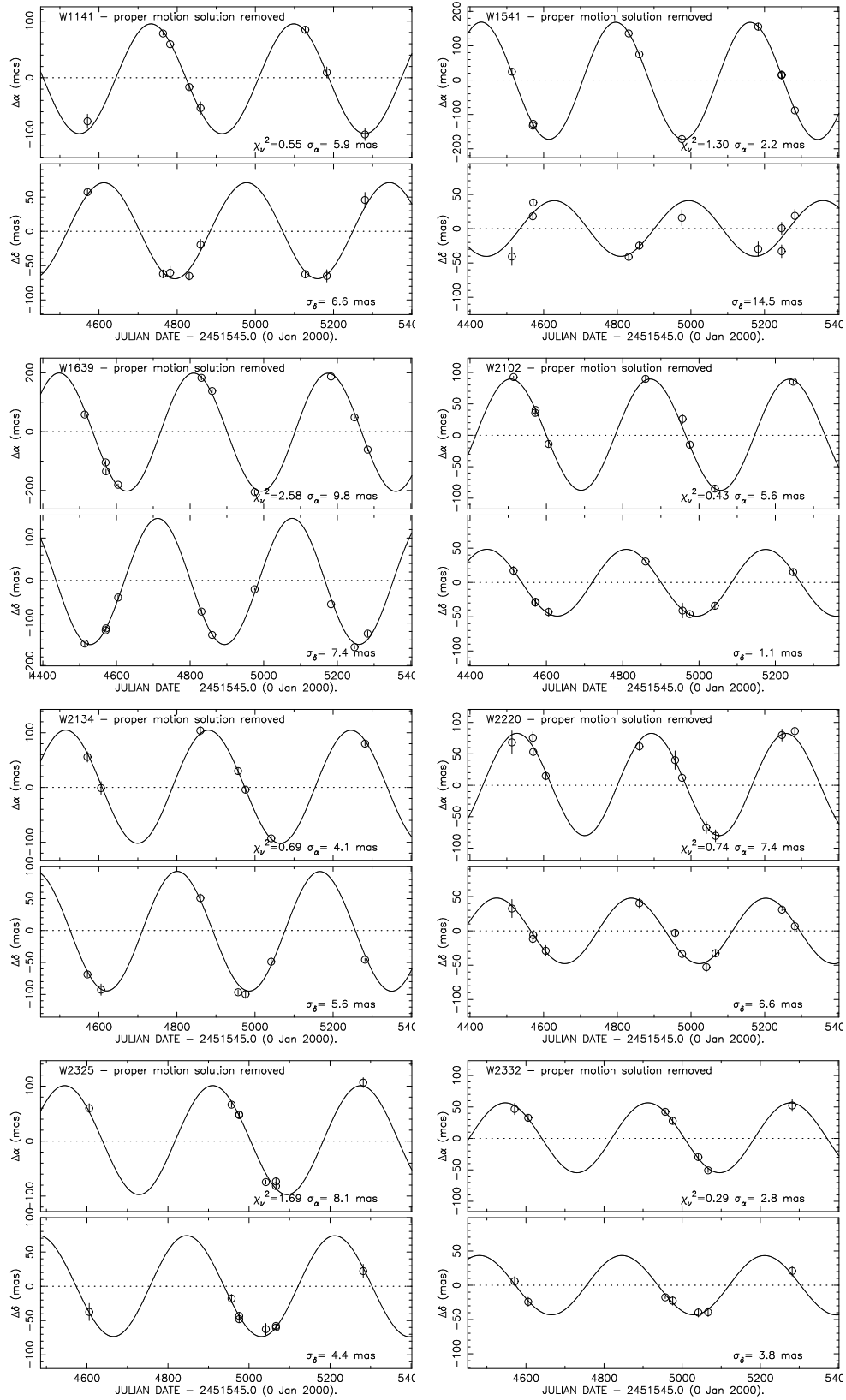


FIG. 2 (CONT.).— Astrometric solutions as reported in Table 2, with the fitted proper motion removed for clarity.

ter photometry (e.g. Leggett *et al.* 2013). Whenever the latter is available we have preferred it in the Table. For w0855 we use the 2.6σ J3 detection of Faherty *et al.* (2014) to estimate a J_{MKO} magnitude, and adopt the uncontaminated W2 magnitude and updated parallax from Wright *et al.* (2014). In the absence of any spectrum for W0855, we assign it a spectral type of $>Y2$ (similar to that assigned to W1828) based on its very faint M_{W2} and extremely red J–W2 colour ($J-W2 = 11.1\pm 0.5$).

We now consider the overlap between our new data and comparable, extant Y dwarf parallaxes summarised in Table 2. We do not, however, compare with the results in Marsh *et al.* (2013) – while that astrometry was the best available at the time of publication, it is not comparable in precision to that being examined here.

B14: We have three objects in common with B14: W0713 for which we measure $\pi=108.7\pm 4.0$ mas compared with B14’s 106 ± 13 mas; W1541 for which we measure $\pi=175.1\pm 4.4$ mas compared with B14’s 176 ± 9 mas; and W2220 for which we measure $\pi=87.2\pm 3.7$ mas compared with B14’s 106 ± 24 mas. In each case our solution is formally consistent (at the combined $1-\sigma$ level) with that of B14. Our quoted uncertainties are smaller, which is to be expected given the per-epoch precisions obtained from the *Spitzer* data that dominate the B14 solutions, where the average precision per epoch of 60 mas compares with the median precision for our targets of 9.9 mas.

K13: have presented a parallax for W0647 of 115 ± 12 mas, while we measure $\pi=93\pm 13$ mas, making the two solutions consistent at the combined $1-\sigma$ level. Our parallax is a preliminary one based on 4 epochs (though those epochs are well placed to measure a robust parallax). The addition of extra epochs over the coming 12 months will see this result become significantly better than is possible with *Spitzer*-based data.

D&K13: We have two objects in common with D&K13: W1541 for which we measure $\pi=175.1\pm 4.4$ mas compared with D&K13’s 74 ± 31 mas; and W0148 for which we measure $\pi=91.1\pm 2.4$ mas compared with D&K’s 60 ± 16 mas. The difference for W1541 is formally a greater than $3-\sigma$ one, which we ascribe to the degeneracy present in the D&K13 solution because it is based on only 3 well-separated epochs (see their Fig. S1), with the earliest and poorest epoch primarily determining the proper motion in their solution, while the later epochs constrain the parallax. The result is a solution with a large relative uncertainty, and significant degeneracy between the proper motion and parallax parameters. Our own data is completely inconsistent with a parallax as small as 70 mas, and is in agreement with the larger parallax reported by B14. We therefore do not plot the D&K13 result for W1541 or report it in the Tables in this paper.

The situation for W0148 (where the difference is formally a 1.9σ one) shares some similarities with that for W1541 in that D&K13 report only 4 widely separated epochs and again the earliest (and by far the poorest epoch) must strongly determine the proper motion solution, generating the possibility of degeneracy between the proper motion and parallax. However, we do not consider the 1.6σ difference between the solutions to be significant enough to warrant rejecting either, and so report and plot both values in the Tables and Figures.

W1639: A preliminary parallax of 200 ± 20 mas for W1639 was previously reported by us (Tinney *et al.* 2012). The uncertainty in that measurement was artificially inflated to account for the added systematic uncertainties introduced by the need to combine early FourStar data with astrometry from the WISE satellite itself. Our new measurement of 202.3 ± 3.1 mas (based on FourStar data only) confirms the previous measurement, and improves the precision significantly.

4. DISCUSSION

4.1. Spectral Type – Absolute Magnitude Diagrams

Absolute magnitudes for the Magellan objects in J_{MKO} (generated from our J3 photometry as described in §2.1) and W2 are plotted as a function of spectral type in Figure 3, along with the comparison data described in §3.1. Table 2 shows median and root-mean-square (rms) absolute magnitudes for each spectral subclass (with the exception of W1141 which has only an estimated spectral type).

There is substantial scatter about the median spectral type versus absolute magnitude sequences. It has to be remembered that typical uncertainties on these spectral classifications are ± 0.5 sub-types – an uncertainty that could allow W0734’s over-luminous absolute magnitude to be consistent with an earlier type of T9.5 (rather than its current Y0 classification), and W1639’s sub-luminous absolute magnitude to be consistent with a later type of Y0.5 (rather than Y0).

An unusually narrow range of luminosities has previously been reported for Y0 dwarfs by D&K13, however the data in Fig. 3 and Table 2 does not reproduce this. Our larger sample of Y0 dwarfs have a substantial rms of 1.05 and a span of 4.2 magnitudes at J. The equivalent figures at W2 are smaller, but still significant (0.32 and 1.2). It could be argued that a few outliers amongst the Y0 brown dwarfs (W2209, W1405, W1639) are skewing this distribution. However we note that the removal of these three still leaves an rms of 0.44 in absolute magnitude at J and 0.23 in absolute magnitude at MW2. We return to this issue below in the context of examining the colour magnitude diagrams.

Finally, we note that this larger sample of parallaxes also shows no conclusive evidence for a brightening of absolute magnitudes for T9.5 objects compared to T9 ones as has been previously reported (Dupuy & Kraus 2013). The data are consistent (especially when the significant scatter about the median values in each bin are considered) with objects becoming monotonically fainter from T through Y (with the possible exception of objects later than Y0.5, as discussed further below).

4.2. Colour – Absolute Magnitude Diagrams

Spectral types do not naturally emerge from theory (i.e. from model atmospheres), as they are a fundamentally empirical classification system driven by observed spectra. The *fluxes* produced by models, however, are robustly tested by colour-magnitude diagrams. The passbands with the most complete and uniform data for late-T and Y dwarfs are the mid-infrared WISE W2 band (where all but one of the known Y dwarfs were discovered) and the near-infrared J passband (where much WISE follow-up imaging has been done). We therefore

TABLE 3
PHOTOMETRIC AND ASTROMETRIC DATA ON T AND Y DWARFS WITH PUBLISHED PARALLAXES^a

Shorthand Designation	<i>AllWISE</i> Designation	SpT	π (mas)	J_{MKO} (mag)	W2 (mag)	SpT Ref	π Ref	Phot Ref	Disc Ref
Y and Late-T dwarfs									
W0146	WISEA J014656.66+423409.9	Y0	94±14	19.40±0.25	15.083±0.065	1	11	1	4
W0148	WISEA J014807.34-720258.7	T9.5	60±16	18.96±0.07	14.592±0.039	2	12	2	4
W0254	WISEA J025409.55+022358.5	T8	135±15	16.14±0.12	12.758±0.026	2	12	3	2,37
W0313	WISEA J031326.00+780744.3	T8.5	153±15	17.67±0.07	13.263±0.026	2	11	1	2
W0335	WISEA J033515.07+431044.7	T9	70±9	20.07±0.30	14.515±0.055	4	11	4	4
W0410	WISEA J041022.75+150247.9	Y0	160±09 132±15	19.44±0.03	14.113±0.047	5	11	21	2,5
W0647	WISEA J064723.24-623235.4	Y1	115±12	22.65±0.27	15.224±0.051	32	32	32	32
W0713	WISEA J071322.55-291752.0	Y0	106±13	19.64±0.15	14.462±0.052	1	11	1	1
W1311	WISEA J131106.21+012253.9	T9	62±12	18.75±0.07	14.703±0.060	2	11	2	2
W0855	WISE J085510.83-071442.5	(>Y2) ^b	448±33	25.00 ^{+0.53} _{-0.35}	14.02±0.05		47	47	35
W1405	WISEA J140518.32+553421.3	Y0p	129±19	21.06±0.06	14.097±0.037	5	12	21	2,5
W1541	WISEP J154151.65-225025.2	Y0.5	176±9	21.12±0.06	13.982±0.112	5	11	21	2,5
W1542	WISEA J154214.00+223005.2	T9.5	96±41	20.25±0.13	15.043±0.061	4	11	4	4
W1738	WISEA J173835.52+273258.8	Y0	128±10 102±18	20.05±0.09	14.497±0.043	5	11	21	2,5
W1741	WISEA J174124.22+255319.2	T9	180±15	16.18±0.02	12.347±0.023	2	12	2	2,37
W1804	WISEA J180435.37+311706.2	T9.5:	80±10 60±11	18.67±0.04	14.590±0.046	2	11	2	2
W1828	WISEA J182831.08+265037.6	>Y2	106±7 70±14	23.48±0.23	14.353±0.045	1	11	21	2,5
W2056	WISEA J205628.88+145953.6	Y0	140±09 144±23	19.43±0.04	13.839±0.037	5	11	21	2,5
W2209	WISEA J220905.75+271143.6	Y0:	147±11	22.58±0.14	14.770±0.055	33	11	33	2
W2220	WISEA J222055.34-362817.5	Y0	106±24	20.38±0.17	14.714±0.056	1	11	1	1
Reference T dwarfs									
U0034	ULAS J003402.77-005206.7	T8.5	68.7±1.4	18.15±0.03	14.500±0.079	6,5	13	6	6
2M0034	2MASS J00345157+0523050	T6.5	105±8	15.11±0.03	12.520±0.028	7	14	10	39
2M0050	2MASS J00501994-3322402	T7	94.6±2.4	15.65±0.10	13.550±0.036	7	13	15	38
CF0059	CFBDS J005910.90-011401.3	T8.5	103.2±2.1	18.06±0.03	13.681±0.043	5	13	23	23
2M0243	2MASS J0243137-245329	T6	94±4	15.13±0.03	12.923±0.027	7	15	24	40
2M0415	2MASS J0415195-093506	T8	175.2±1.7	15.32±0.03	12.261±0.026	7	13	24	40
2M0559	2MASS J0559191-140448	T4.5	96.6±1.0	13.57±0.03	11.904±0.023	7	13	28	41
U0722	UGPS J072227.51-054031.2	T9	242.8±2.4	16.52±0.02	12.213±0.027	5	16	25	25
2M0727	2MASS J0727182+171001	T7	112.5±0.9	15.19±0.03	12.962±0.033	7	13	24	40
2M0729	2MASS J07290002-3954043	T8p	126±8	15.64±0.08	12.964±0.026	8	14	26	8
U0901	ULAS J090116.23-030635.0	T7.5	62.6±2.6	17.90±0.04	14.604±0.074	9	17	9	9
2M0939	2MASS J09393548-2448279	T8	187±5	15.61±0.09	11.639±0.022	7	18	27	38
2M1007	2MASS J10073369-4555147	T5	71±5	15.42±0.07	13.870±0.040	8	14	26	8
2M1047	2MASS J1047538+212423	T6.5	95±4	15.46±0.03	12.972±0.032	7	15	28	42
S1110	SDSS J111010.01+011613.1	T5.5	52.1±1.2	16.12±0.05	13.917±0.047	7	13	28	43
2M1114	2MASS J11145133-2618235	T7.5	179.2±1.4	15.52±0.05	12.239±0.026	7	13	22	38
2M1217	2MASS J1217110-031113	T7.5	90.8±2.2	15.56±0.03	13.197±0.035	7	19	28	42
2M1237	2MASS J12373919+6526148	T6.5	96±5	15.56±0.10	12.946±0.027	7	15	22	42
U1335	ULAS J133553.45+113005.2	T8.5	99.9±1.6	17.90±0.01	13.865±0.042	5	13	29	29
S1346	SDSSp J134646.45-003150.4	T6.5	68.3±2.3	15.49±0.05	13.567±0.034	7	19	30	30
G1570D	G1570D	T7.5	171.2±0.9	14.82±0.05	12.114±0.023	7	20	34	44
2M1503	2MASSW J1503196+252519	T5	157.2±2.2	13.55±0.03	11.723±0.021	7	13	24	45
S1504	SDSS J150411.63+102718.3	T7	46.1±1.5	16.49±0.03	14.062±0.040	10	13	10	10
2M1546	2MASS J15462718-3325111	T5.5	88.0±1.9	15.41±0.05	13.445±0.037	7	19	26	40
2M1615	2MASS J16150413+1340079	T6	69±6	16.11±0.09	14.194±0.053	8	14	26	8
S1624	SDSSp J162414.37+002915.6	T6	90.9±1.2	15.20±0.05	13.085±0.032	7	19	31	31
S1628	SDSS J162838.77+230821.1	T7	75.1±0.9	16.25±0.03	13.961±0.043	10	13	10	10
S1758	SDSS J175805.46+463311.9	T6.5	71.0±1.9	15.86±0.03	13.823±0.032	7	20	24	24
2M1828	2MASS J18283572-4849046	T5.5	84±8	14.94±0.06	12.773±0.029	7	14	26	39
2M2228	2MASS J22282889-4310262	T6	94±7	15.42±0.07	13.328±0.035	7	14	26	46
2M2356	2MASS J2356547-155310	T5.5	69±3	15.48±0.03	13.708±0.042	7	15	24	40

REFERENCES. — 1 - Kirkpatrick et al. (2012); 2 - Kirkpatrick et al. (2011); 3 - Liu et al. (2011a); 4 - Mace et al. (2013); 5 - Cushing et al. (2011); 6 - Warren et al. (2007); 7 - Burgasser et al. (2006); 8 -Looper et al. (2007); 9 - Lodieu et al. (2007); 10 - Chiu et al. (2006); 11 - Beichman et al. (2014); 12 - Dupuy & Kraus (2013); 13 - Dupuy & Liu (2012); 14 - Faherty et al. (2012); 15 - Vrba et al. (2004); 16 - Leggett et al. (2012); 17 - Marocco F. et al. (2010); 18 - Burgasser et al. (2008); 19 - Tinney et al. (2003); 20 - van Leeuwen et al. (2007); 21 - Leggett et al. (2013); 22 - Leggett et al. (2010); 23 - Delorme et al. ; 24 - Knapp et al. (2004); 25 - Lucas et al. (2010); 26 - Synthetic photometry derived from literature spectra by Trent Dupuy (https://www.cfa.harvard.edu/~tdupuy/plx/Database_of_Ultracool_Parallaxes.html); 27 - Leggett et al. (2009); 28 - Leggett et al. (2002); 29 - Burningham et al. (2008); 30 - Tsvetanov et al. (2000); 31 - Strauss M.A. et al. (1999); 32 - Kirkpatrick et al. (2013); 33 - Cushing et al. (2014b); 34 - Geballe et al. (2001); 35 - Luhman (2014); 36 - Faherty et al. (2014); 37 - Scholz et al. (2011); 38 - Tinney et al. (2005); 39 - Burgasser et al. (2004); 40 - Burgasser et al. (2002); 41 - Burgasser et al. (2000b); 42 - Burgasser et al. (1999) Burgasser, A. J., Kirkpatrick, J. D., Brown, M. E., et al. 1999, ApJ, 522, L65; 43 - Geballe et al. (2002); 44 - Burgasser et al. (2000a); 45 - Burgasser et al. (2003a); 46 - Burgasser et al. (2003b); 47 - Wright et al. (2014)

^aSpectral type (SpT), parallax (π) and photometry in the J_{MKO} and *AllWISE* W2 passbands. No spectrum has been published for W0855, so its type estimate (>Y2) is based on the lower limit to its J–W2 colour, together with its very low luminosity in W2 and J.

^bThe upper limit to the spectral type for W0855 is an estimate based on its photometry and extremely faint absolute magnitude.

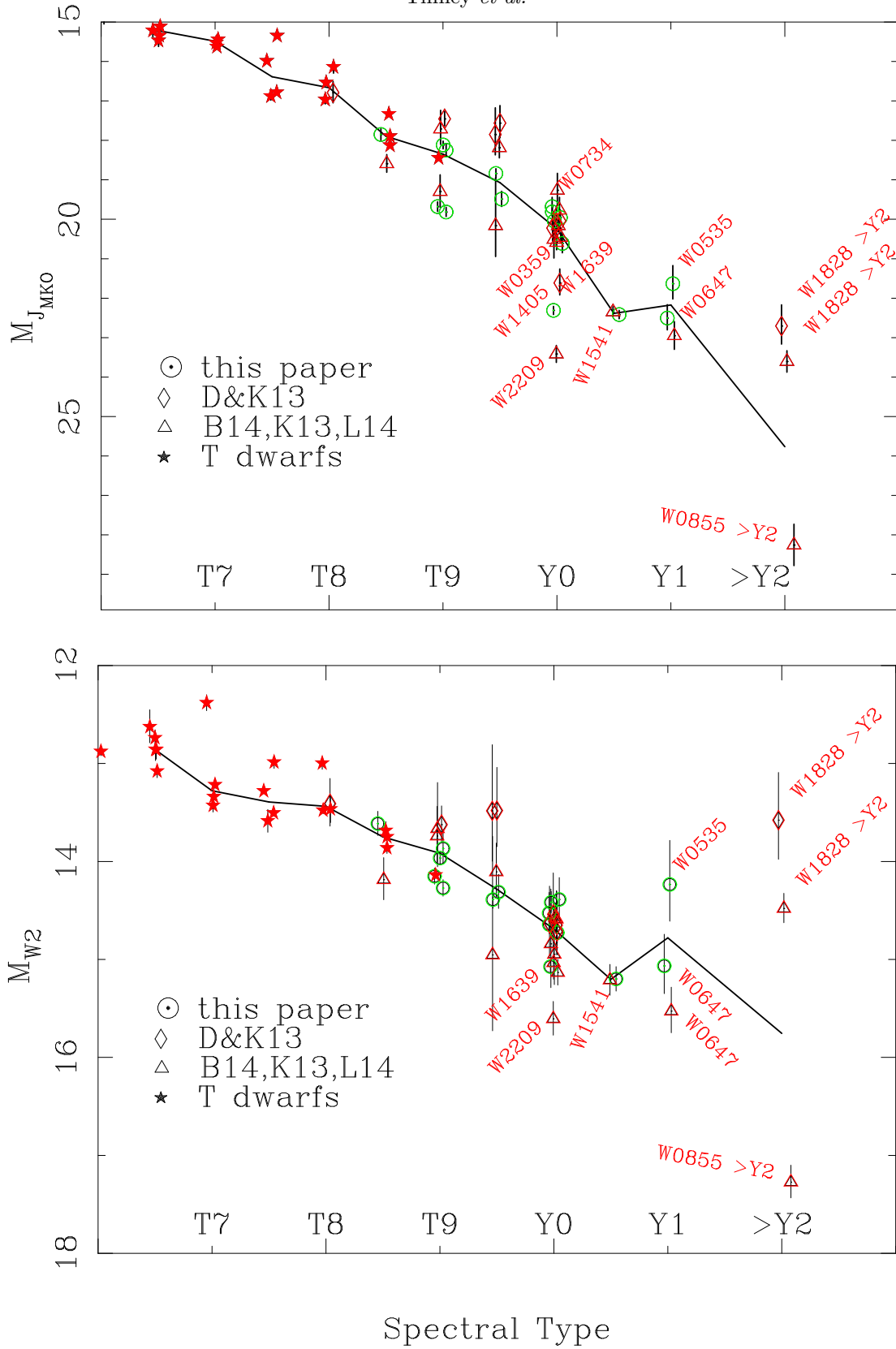


FIG. 3.— Absolute magnitude in the J_{MKO} and $W2$ passbands as a function of spectral types for Y dwarfs presented in this paper (green open circles), by Dupuy & Kraus (2013, D&K13 – red open diamonds) and Beichman *et al.* (2014); Kirkpatrick *et al.* (2013, B14, K13 – red open triangles) and for a reference sample of T dwarfs (red solid stars). Where multiple distances have been measured for a target, we plot each independently. Each data point has had a small random offset in spectral type applied to make the plot clearer. The solid line shows the median magnitude for all measurements at each spectral type. Table 2 summarises the scatter about that line at each spectral type. Selected objects are highlighted where this can be done with clarity. The exception is W0359 which lies at the lower edge of a cluster of Y0s near $M_J=20$. This is in contrast to its isolated position in the colour magnitude diagrams in Figure 4.

TABLE 4
COMPARISON WITH LITERATURE PARALLAXES.

Object	π (mas) This paper	π (mas) B14	π (mas) K13	π (mas) D&K13
W0148	91.1±2.4	60±16
W0647	93±13	...	115±12	...
W0713	108.7±4.0	106±13
W1541	175.1±4.4	176±9	...	74±31
W2220	87.2±3.7	106±24

REFERENCES. — B14 – Beichman et al. (2014); K13 – Kirkpatrick et al. (2013); D&K13 – Dupuy & Kraus (2013).

TABLE 5
MEDIAN AND RMS ABSOLUTE MAGNITUDES OF ALL
INDEPENDENT OBSERVATIONS OF LATE T AND Y DWARFS,
BINNED BY SPECTRAL TYPE (SpT).

SpT	N ^a	M _J median	M _J rms	M _{W2} median	M _{W2} rms
T6.5	5	15.22	0.31	12.86	0.17
T7.0	4	15.49	0.37	13.28	0.48
T7.5	4	16.39	0.72	13.39	0.27
T8.0	4	16.66	0.36	13.44	0.23
T8.5	5	17.90	0.46	13.75	0.22
T9.0	8	18.35	0.90	13.92	0.24
T9.5	4	19.08	0.97	14.28	0.46
Y0.0	11	20.32	1.25	14.65	0.35
Y0.5	1	22.39	...	15.20	...
Y1.0	2	22.18	0.76	14.78	0.77
>Y2.0 ^b	2	25.76	3.52	15.76	2.15

^a – N is the number of independent distance measurements in each bin. Where multiple distances are available for a single target, they are combined in a weighted fashion before calculating these statistics. W1141, which does not have a spectral type, is not included in these calculations.

^b The >Y2 category contains only two members in this table and may well represent a range in spectral types - the median and rms likely reflect this diversity.

show J_{MKO} and W2 colour-magnitude diagrams in Fig. 4. As we show below these diagrams have the advantage of having minimal sensitivity to gravity.

Some objects classified as Y0 have absolute magnitudes and colours consistent with types different to those assigned by their spectra. W0734, for example, lies at an absolute magnitude and colour consistent with being a late T dwarf (rather than a Y dwarf), while W1639 and W2209 lie at locations suggesting photometric properties and effective temperatures more in common with Y1 (and later) brown dwarfs than Y0 ones. These are reflected in the spectral-type-verses-absolute-magnitude diagrams presented in Fig. 3 (as noted above). This scatter could also reflect metallicity variations at the 0.3 dex level as indicated by benchmark studies of T dwarfs (Burningham et al. 2013).

The challenge posed by the molecular physics, cloud formation physics and radiative transfer for atmospheric models at these temperatures is considerable, and multiple generations of models have been required to reproduce observed properties. The most straightforward are “cloudless” models, which assume that condensed materials drop to layers below the photosphere and so are removed from the radiative transfer. “CldFree” models

TABLE 6
DEVIATIONS FROM CLOUD FREE $\log g = 5.0$ MODEL

J-W2 range	N	ΔM_{W2} ^a mean	ΔM_{W2} rms
3.0-4.0	7	0.12	0.42
4.0-5.0	11	0.05	0.35
5.0-6.0	12	-0.13	0.40
6.0-7.0	2	-0.62	0.01
7.0-8.0	5	-0.34	0.49
8.0-11.5	2	-0.66	1.60

^aMean and rms values for the difference (ΔM_{W2}) between the observed absolute magnitude and the model W2 absolute magnitude for each object’s J–W2 (in the sense $\Delta M_{W2} = \text{“observation”} - \text{“model”}$). Where multiple distances are available for a single target, they are combined in a weighted fashion before calculating these statistics.

are shown in Fig. 4 due to Saumon et al. (2012) based on models by Morley et al. (2012); Saumon & Marley (2008) and also presented in Leggett et al. (2013). These are shown in the figure for surface gravities of $\log g = 4.0$ and 5.0 (the range relevant for brown dwarfs of age 100Myr–10Gyr with masses 5–30 M_{Jup} ; Baraffe et al. 2003). The impact of this plausible spread in gravities is small – ≈ 0.5 mag in M_J and M_{W2} for T_{eff} above 400K, dropping to less than 0.1 mag for T_{eff} at 300K and cooler. Moreover, the impacts of gravity in both passbands are of a similar magnitude and operate in the same direction, so that for a given J–W2 colour, there is very little sensitivity to gravity predicted by the models.

The agreement between these cloudless models and the lower envelope of observed absolute magnitudes is generally good. Table 2 summarises the median and rms values (binned in J–W2) for the difference ΔM_{W2} between the $\log g=5.0$ model and the observed M_{W2} for each object. Given these models are a *prediction* (not a fit) the agreement is striking, especially considering the complexity of the models and the history of poor matches between predictions and observations in this field.

That being said, some Y dwarfs are over-luminous in J_{MKO} and W2 compared to these models. W0359 (Y0), W1405 (Y0) and W0535 (Y1) sit 0.6, 0.6 and 1.1 mag (respectively) above the “CldFree” $\log(g)=5.0$ model, which otherwise fits the sequence of late T and Y dwarfs well. W0335 is a T9 dwarf that appears similarly over-luminous (by 1.0 mag). The >Y2 object W1828 is even more over-luminous. This is a long-standing issue to which we return below.

No plausible range of brown dwarf radii can produce gravity variations sufficient to explain this over-luminosity. Unresolved binarity could be the cause, since an unrecognized equal-mass binary delivers an absolute magnitude excess of 0.75 mag. For the distances at which these objects lie (7.5–15.6 pc), adaptive optics imaging on 8m-class telescopes will deliver the ability to detect binaries at separations down of much less than 1au and test this hypothesis within a few years.

An alternative explanation is that this over-luminosity could be due to cloud formation. Clouds are known to form in brown dwarfs at higher temperatures, and expected to form at the temperature ranges in question here (450–300K), and variability suggestive of clouds has

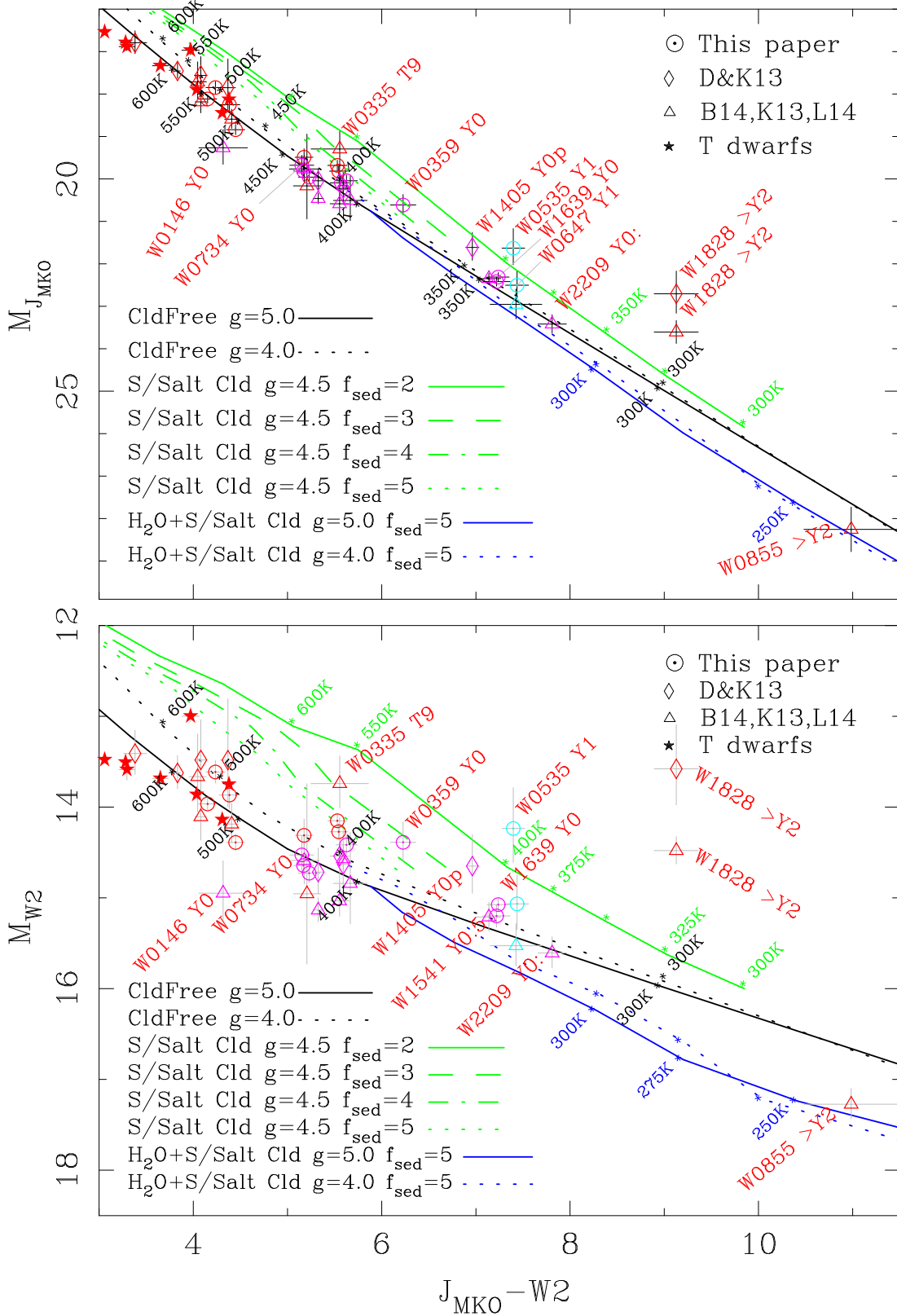


FIG. 4.— Colour–Absolute Magnitude diagrams in the J_{MKO} and W2 passbands. Symbols are as for Fig.3 except that Y0/Y0.5 objects are coloured magenta and Y1 cyan. Where multiple distances have been measured for a target, we plot each independently. Cloudless models (labelled “CldFree”, black lines, Saumon *et al.* 2012) are superimposed at $\log g = 4.0$ and 5.0 , along with Sulfide+Salt cloud models (“S/Salt Cld”, green lines, Morley *et al.* 2012) at $\log g = 4.5$ for $f_{\text{sed}} = 2-5$ – with the $f_{\text{sed}} = 2$ model extended by a special model run to $T_{\text{eff}}=300\text{K}$, and water cloud models due to Morley *et al.* (“H₂O+S/Salt Cld”, blue lines, 2014) with $\log g = 5.0$ and 4.0 at $f_{\text{sed}} = 5$.

been reported in *Spitzer* observations for at least one Y dwarf (Cushing et al. 2014a).

Cloud decks in multiple species have been predicted, with two classes of clouds predicted to be particularly likely: sulfide and salt condensates (including Cr, MnS, Na₂S, ZnS and KCl), and H₂O clouds. Models for the former have been presented by Morley et al. (2012), by balancing the upward transport of vapor and condensate by turbulence, with the downward transport of condensate by sedimentation, the effects of which are determined by a parameter f_{sed} that describes the efficiency of sedimentation. High f_{sed} models have vertically thinner clouds with larger particle sizes (i.e. optically thinner clouds), whereas low f_{sed} models have more vertically extended clouds with smaller particles (i.e. optically thicker clouds). The predicted tracks for these ‘‘S/Salt Cld’’ models at $\log(g)=4.5$ for a range of f_{sed} values are also shown in Fig. 4 (with the $f_{\text{sed}}=2$ tracks extended to temperatures of 300K to demonstrate their potential impact at very low temperatures).

These models do not include the effects of H₂O ice clouds, which will become more important at temperatures below 400K (Morley et al. 2012). Morley et al. (2014) have modelled the additional impact of these clouds and they are shown in Fig. 4 as ‘‘H₂O+S/Salt Cld’’ tracks for $f_{\text{sed}}=5$ at $\log(g)=4.0$ and 5.0. The impact of these two types of cloud are quite distinct – sulphide and salt clouds make models at equivalent effective temperatures redder in J–W2, so that the models appear to sit at higher luminosities in Fig. 4 compared to Cloudless tracks. H₂O clouds, on the other hand, make models at equivalent effective temperatures bluer in J–W2, so that these model tracks appear to sit at lower luminosities than Cloudless models.

The sulphide and salt clouds redden J–W2 because they reside deep in the atmosphere. The J band lies in a window between molecular absorption features in which we usually see very deeply, however clouds limit the depth to which we observe, decreasing the J band flux. The W2 flux emerges from higher altitudes, well above the salt/sulfide clouds, so W2 changes very little. In comparison, the water ice clouds are formed higher in the atmosphere where the mid-infrared flux emerges. In addition, the optical properties of water ice mean that it absorbs much more strongly in the mid-infrared than in the optical-through-J band (where it scatters but absorbs little). This means that we see a similar flux emerging in the J band, but a decreased flux in W2, making the models appear bluer in J–W2.

In the main, most of the Y dwarfs with distance measurements are consistent with cloud-free model predictions. Nonetheless a few Y dwarfs display an over-luminosity in the near-infrared that could be caused (assuming they are not shown to be binaries) by the presence of thick clouds of sulphide and salt condensates at temperatures of 400K or below. In contrast, W0855 (Luhman 2014) lies in a region of the colour magnitude diagram (extremely red in J–W2 and sub-luminous for its colour in M_{W2}) requiring the presence of water

ice clouds, making it the first system to display this behaviour (Faherty et al. 2014).

None of the models predict the over-luminosity of W1828, which remains an enigma. In particular, the suggestion that this system could be a 325K+300K binary (Leggett et al. 2013) seems hard to reconcile with it being observed to lie 2 magnitudes above the Cloudless model sequence in M_{W2} (Fig. 4), 2.5 magnitudes brighter than the H₂O Cloudy model sequence, and 3.2 magnitudes brighter than W0855 (which is otherwise consistent with the H₂O Cloudy model sequence). For W1828’s over luminosity relative to both W0855 and these models to be explicable by binarity, it would have to be an nearly-equal-mass-triple or -quadruple system. Between them W1828 and W0855 certainly indicate that even the coldest brown dwarfs currently known display a large spread in absolute magnitude for a given colour.¹⁴

The fact that some Y dwarfs are significantly over-luminous (for a given colour), while others are not, suggests the extent of cloud coverage could vary significantly between otherwise similar Y dwarfs. This would either imply that cloud *thickness*, or that *cloud coverage* varies. The latter would mean that cloud sensitive photometric or spectroscopic features can be expected to vary as these objects rotate. Precisely this type of variability has been seen at the L–T spectral type transition (Radigan et al. 2012; Artigau et al. 2009; Crossfield et al. 2014), for mid-T dwarfs (Buenzli et al. 2014), and is predicted in late T dwarfs (Morley et al. 2012) due to sulphide and salt clouds. Recent *Spitzer* results indicate some Y dwarfs are indeed variable on timescales suggesting the presence of clouds (Cushing et al. 2014a). It will be important (despite the severe technical challenges posed by these faint targets) to target Y dwarf variability as a probe of their cloud structures and properties.

This paper includes data gathered with the 6.5 meter Magellan Telescopes located at Las Campanas Observatory, Chile. Australian access to the Magellan Telescopes was supported through the National Collaborative Research Infrastructure and Collaborative Research Infrastructure Strategies of the Australian Federal Government. Access through the Chilean Time Allocation Committee was supported by awards CN2012A-011, CN2012B-057, CN2013A-127. This research was supported by Australian Research Council grants DP0774000 and DP130102695. This publication makes use of data products from the Wide-field Infrared Survey Explorer (WISE), which is a joint project of the University of California, Los Angeles, and the Jet Propulsion Laboratory/California Institute of Technology, and NEOWISE, which is a project of the Jet Propulsion Laboratory/California Institute of Technology. WISE and NEOWISE are funded by the US National Aeronautics and Space Administration.

Facilities: Magellan:Baade (FourStar), WISE

REFERENCES

- Allard, F., Guillot, T., Ludwig, H.-G., et al. 2003, in IAU Symposium 211, Brown Dwarfs, ed. E. Martin (San Francisco, CA: ASP), 325
- Artigau, E., Bouchard, S., Doyon, R., & Lafreniere, D. 2009, ApJ, 701, 1534

- Baraffe, I., Chabrier, G., Barman, T., Allard, F., Hauschildt, P. 2003, *A&A*, 402, 701
- Beichman, C., Gelino, C. R., Kirkpatrick, J. D., Cushing, M. C., Dodson-Robinson, S., Marley, M.S., Morley, C. V., Wright, E. L., 2014, *ApJ*, 783, 68 (B13)
- Bertin, E. & Arnouts, S., *A&AS*, 117, 393
- Buenzli, E., Apai, D., Radigan, J., Reid, I. N., Flateau, D., 2014, *ApJ*, 782, 77
- Burgasser, A. J., Kirkpatrick, J. D., Brown, M. E., et al. 1999, *ApJ*, 522, L65
- Burgasser, A. J., Kirkpatrick, J. D., Brown, M. E., et al. 2002, *ApJ*, 564, 421
- Burgasser, A. J., Kirkpatrick, J. D., Cruz, K. L., Reid, I. N., Leggett, S. K., Liebert, J., Burrows, A., Brown, M. E. 2006, *ApJS*, 166, 585
- Burgasser, A. J., Kirkpatrick, J. D., Cutri, R. M., et al. 2000a, *ApJ*, 531, L57
- Burgasser, A. J., Kirkpatrick, J. D., McElwain, M. W., et al. 2003a, *AJ*, 125, 850
- Burgasser, A. J., McElwain, M. W., Kirkpatrick, J. D. 2003b, *AJ*, 126, 2487
- Burgasser, A. J., McElwain, M. W., Kirkpatrick, J. D., et al. 2004, *AJ*, 127, 2856
- Burgasser, A. J., Tinney, C. G., Cushing, M. C., et al. 2008, 689, L53
- Burgasser, A. J., Wilson, J. C., Kirkpatrick, J. D., et al. 2000b, *AJ*, 120, 1100
- Burningham, B., Pinfield, D. J., Leggett, S. K. et al. 2008, *MNRAS*, 391, 320
- Burningham, B. et al. 2013, *MNRAS*, 433, 457
- Chiu, K., Fan, X., Leggett, S. K., Golimowski, D. A., Zheng, W., Geballe, T. R., Schneider, D. P., Brinkmann, J., 2006, *ApJ*, 131, 2722
- Crossfield, I.J.M et al. 2014, *Nature*, 505, 654
- Cushing, M. C., Kirkpatrick, J. D., Gelino, C. R., et al. 2011, *ApJ*, 743, 50
- Cushing, M., Hardegree-Ullman, K., Trucks, J, 2014a, *AAS*, 223, 425.08
- Cushing, M. C., Kirkpatrick, J. D., Gelino, C. R., Mace, G. N., Skrutskie, M. F., Gould, A., 2014b, *AJ*, 147, 113
- Dahn, C. C., Harris, H. C., Vrba, F. J. et al. 2002, *AJ*, 124, 1170
- Delorme, P., Delfosse, X., Albert, L. et al. 2008, *A&A*, 482, 961
- Dupuy, T. J. & Kraus, A. L. 2013, 2013, 341, 1492 (DK13)
- Dupuy, T. J. & Liu, M. C. 2012, *ApJS*, 201, 19
- Faherty, J. K., Burgasser, A. J., Walter, F. M. et al., 2012, *ApJ*, 752, 56
- Faherty, J. K., Tinney, C. G., Monson, A. et al., 2014, *ApJL*, 793, L16
- Geballe, T. R., Saumon, D., Leggett, S. K., Knapp, G. R., Marley, M. S., Lodders, K., 2001, *ApJ*, 556, 373
- Geballe, T. R., Knapp, G. R., Leggett, S. K., et al. 2002, *ApJ*, 564, 466
- Kirkpatrick, J. D., Cushing, M. C., Gelino, C. R., et al. 2011, *ApJS*, 197, 19
- Kirkpatrick, J. D., Gelino, C. R., Cushing, M. C., et al. 2012, *ApJ*, 753, 156
- Kirkpatrick, J. D., Cushing, M. C., Gelino, C. R. et al. 2013, *ApJ*, 776, 128 (K13)
- Knapp, G. R., Leggett, S. K., Fan, X. et al., 2004, *ApJ*, 127, 3553
- Leggett, S. K., Burningham, B., Saumon, D. 2010, *ApJ*, 710, 1627
- Leggett, S. K., Cushing, M. C., Saumon, D. et al. 2009, *ApJ*, 695, 1517
- Leggett, S. K., Golimowski, D. A., Fan, X. et al. 2002, *ApJ*, 564, 452
- Leggett, S. K., Saumon, D., Marley, M. S., et al. 2012, *ApJ*, 748, 74
- Leggett, S. K., Morley, C.V., Marley, M.S., Saumon, D., Fortney, S.J., Visscher, C., 2013, *ApJ*, 763, 130
- Liu, M. C., Deacon, Niall R., Magnier, E. A. et al. 2011a, *ApJ*, 740, L32
- Liu, M. C., Delorme, P. Dupuy, T.J. et al. 2011b, *ApJ*, 740, 108
- Lodieu, N., Pinfield, D. J., Leggett, S. K. et al., 2007, *MNRAS*, 379, 1423
- Looper, D. L., Kirkpatrick, J. D., & Burgasser, A. J. 2007, *AJ*, 134, 1162
- Lucas, P. W., Tinney, C. G., Burningham, B. et al. 2010, *MNRAS*, 408, L56
- Luhman, K.L., 2014, *ApJ*, 786, L18 (L14)
- Luhman, K.L., Burgasser, A. J., Bochanski, J. J., 2011, *ApJ*, 730, L9
- Mace, G. N., Kirkpatrick, J. D., Cushing, M. C., et al. 2013, *ApJS*, 205, 6
- Mainzer, A., Bauer, J., Grav, T. et al. 2011, *ApJ*, 731, 53
- Marocco F., Smart R.L., Jones H.R.A., et al. 2010, *A&A*, 524, 38
- Marsh, K. A. et al. 2013, *ApJ*, 762, 119
- Monet, D.G., Dahn, C.C., Vrba, F.J., Harris, H.C., Pier, J.R., Luginbuhl, C.B., Ables, H.D., 1992 *AJ*, 103, 638
- Morley, C. V., Fortney, J. J., Marley, M. S., Visscher, C., Saumon, D. & Leggett, S. K. 2012, *ApJ*, 756, 172
- Morley, C. V., Marley, M. S., Fortney, J. J. et al. 2014, *ApJ*, 787, 78
- Persson, S. E., Barkhouser, R., Birk, C., et al. 2008, *Proc. SPIE*, 7014, 95
- Radigan, J., Jayawardhana, R., Lafreniere, D., Artigau, E., Marley, M., Saumon, D., 2012, *ApJ*, 750, 105
- Reid, I.N.R. & Hawley, S.L. 2006, *New Light on Dark Stars* (Springer:Heidelberg)
- Saumon, D. & Marley M. S. 2008, *ApJ*, 689, 1327
- Saumon, D., Marley, M. S., Abel, M., Frommhold, L., Freedman, R. S., 2012, *ApJ*, 750, 74
- Scholz, R.-D., Bihain, G., Schnurr, O., & Storm, J. 2011, *A&A*, 532, L5
- Skrutskie, M. F., Cutri, R. M., Stiening, R., et al. 2006, *AJ*, 131, 1163
- Smart, R. L., *Mem. S. A. It.* 2014, in press
- Stetson, P.B., 1987, *PASP*, 99, 191
- Stevenson, D. 1991, *ARA&A*, 29, 163
- Strauss M.A., Fan X., Junn J.E. et al. 1999, *ApJ*, 522, 61
- Tinney, C. G., Burgasser, A. J., & Kirkpatrick, J. D. 2003, *AJ*, 126, 975
- Tinney, C. G., Burgasser, A. J., Kirkpatrick, J. D., McElwain, M. W., 2005, *AJ*, 130, 2326
- Tinney, C. G., Reid, I. N., Gizis, J., & Mould, J. R. 1995, *AJ*, 110, 3014
- Tinney, C. G., Faherty, J. K., Kirkpatrick, J. D. et al. 2012, *ApJ*, 759, 60
- Tsuji T. 2000. In *Very Low-Mass Stars and Brown Dwarfs*, ed. R Rebolo, MR Zapatero Osorio, pp. 156–68. Cambridge, UK: Cambridge Univ. Press
- Tsvetanov, Z. I., Golimowski, D. A., Zheng, Wei, 2000, *ApJ*, 531, 61
- Vrba, F. J. et al., 2004, *AJ*, 127, 2948
- Warren, S. J., Mortlock, D. J., Leggett, S. K. et al. 2007, *MNRAS*, 381, 1400
- Wright, E.L. et al. 2010 *AJ*, 140, 1868.
- Wright, E. L., Mainzer, A., Kirkpatrick, J. D., et al. 2014, arXiv:1405.7350
- van Leeuwen, F. 2007, *A&A*, 474, 653

TABLE 2
PHOTOMETRIC & ASTROMETRIC DATA FOR MAGELLAN TARGETS

Designations Short	WISE	SpT	J3 (mag)	JMKO (mag)	W2 (mag)	π (mas)	μ (mas/y)	θ (deg)	V_{tan} km/s	N_{epoch} , N_{ref}	Disc Ref	Phot Ref
W0148	WISEA J014807.34-720258.7	T9.5	18.83±0.02	18.96±0.07	14.592±0.039	91.1±3.4	1269.3±4.1	90.0±0.2	66±13	7,18	2,6	2
W0359	WISEA J035934.07-540154.8	Y0	21.40±0.09	21.56±0.24	15.384±0.054	63.2±6.0	765±12	193.3±0.8	57±18	7,8	4	4
W0535	WISEA J053516.87-750024.6	Y1	22.09±0.07	...	14.904±0.047	74±14	119±16	287.7±3.7	7.7±3.5	5,21	4	4
W0647	WISEA J064723.24-623235.4	Y1	22.45±0.07	22.65±0.27	15.224±0.051	93±13	368±18	0.1±2.5	18.8±7.0	4,37	5	5
W0713	WISEA J071322.55-291752.0	Y0	19.42±0.03	19.64±0.15	14.462±0.052	108.7±4.0	540.2±7.3	139.6±0.1	23.6±4.6	7,21	4	3
W0734	WISEA J073444.03-715743.8	Y0	20.13±0.08	20.41±0.27	15.189±0.050	73.7±6.6	571.6±7.7	261.8±0.8	37±11	7,32	4	4
W0811	WISEA J081117.95-805141.4	T9.5	19.31±0.01	...	14.345±0.038	98.5±7.7	293.4±6.9	100.6±0.9	14.1±4.0	6,19	7	4
W1042	WISEA J104245.24-384238.1	T8.5	18.58±0.02	...	14.556±0.048	64.8±3.4	93.7±6.2	143.3±1.4	6.9±1.6	9,26	6	6
W1141	WISEA J114156.67-332635.5	(Y0) ^a	19.63±0.05	19.76±0.14	14.611±0.055	105.5±4.3	901.0±6.3	264.6±0.4	40.5±8.2	7,20	3	3
W1541	WISEP J154151.65-225025.2 ^b	Y0.5	20.99±0.03	21.12±0.06	13.982±0.112	175.1±4.4	899.0±4.2	264.4±0.3	24.3±3.9	8,23	6	1
W1639	WISEA J163940.84-684739.4	Y0	20.57±0.05	...	13.544±0.059	202.3±3.1	3156.0±3.5	169.3±0.1	73.9±9.2	8,13	8	3
W2102	WISEA J210200.14-442919.9	T9	18.08±0.01	18.24±0.04	14.139±0.043	92.3±1.9	356.9±2.7	173.3±0.3	18.3±2.6	8,18	4	3
W2134	WISEA J213456.79-713744.7	T9p	19.28±0.04	...	13.962±0.036	109.1±3.7	1381.4±6.2	99.3±0.2	60±11	6,21	2	2
W2220	WISEA J222055.34-362817.5	Y0	20.13±0.02	20.47±0.11	14.714±0.056	87.2±3.7	297.9±5.2	108.4±0.5	16.2±3.3	9,22	2	3
W2325	WISEA J232519.55-410535.1	T9p	19.44±0.02	19.75±0.05	14.108±0.040	107.8±3.7	837.0±6.7	91.2±0.6	36.8±6.8	5,16	2	2
W2332	WISEA J233226.54-432510.9	T9	19.13±0.02	19.40±0.10	14.958±0.066	60.5±4.0	355.6±7.4	136.0±0.1	27.9±7.2	6,22	4	3

REFERENCES. — 1 - Leggett et al. (2013), 2 - Kirkpatrick et al. (2011), 3 - C.G. Tinney et al. 2014, in preparation, 4 - Kirkpatrick et al. (2012), 5 - Kirkpatrick et al. (2013), 6 - Cushing et al. (2011), 7 - Mace et al. (2013), 8 - Tinney et al. (2012)

^a The spectral type for W1141 has been estimated from its photometry as described in the text.

^b The parallax solution for W1541 is based on the right ascension solution alone as described in the text.